RSC Advances

PAPER

View Article Online
View Journal | View Issue

Open Access Article. Published on 28 January 2026. Downloaded on 3/7/2026 11:12:56 PM.
This article is licensed under a Creative Commons Attribution-NonCommercial 3.0 Unported Licence.

Check for updates

Cite this: *RSC Adv.*, 2026, **16**, 5877

First-principles screening of dopants for high-conductivity graphene/copper interfaces

Xinsi Zhao,[a] Boan Zhong,[a] Baixue Bian,*[a] Jiamiao Ni,[a] Mingyu Gong,*[ab] Yue Liu*[a] and Tongxiang Fan[a]

Received 25th November 2025
Accepted 20th January 2026

DOI: 10.1039/d5ra09101b

rsc.li/rsc-advances

Chemical doping is one of the promising approaches for tailoring the electronic properties of graphene/copper (Gr/Cu) composites. However, the diversity of doping elements and their complex bonding configurations result in nuanced effects, such as the competition between increased carrier concentration and defect generation (lattice distortion). Therefore, it is essential to decouple such complex doping effects into the intrinsic contribution of the dopant atom and the extrinsic effects of defects like vacancies. In this work, first-principles calculations, deformation potential theory, and the parabolic band model are combined to investigate the intrinsic mechanisms of various dopants. This approach decouples their contributions to carrier concentration and mobility, enabling the effective selection of dopants with optimal carrier transport properties. The corresponding results reveal that dopants which significantly distort the Dirac cone structure, such as O, S, P, Br, and Si, lead to significant degradation of carrier mobility and are thus excluded. In contrast, N is identified as the optimal dopant of Gr/Cu composites, outperforming B by effectively enhancing carrier concentration while well maintaining high carrier mobility, thereby achieving a superior balance for enhanced conductivity. This work establishes a theoretical framework for dopant selection and provides key insights for the design of high-conductivity Gr/Cu composites.

1 Introduction

With the rapid development of modern technology and emerging fields such as integrated circuits (ICs) and high-frequency communication, the requirements for copper (Cu) conductors with ultra-high electrical conductivity have become increasingly stringent. The development of high conductivity Cu foils is crucial for mitigating conductor losses in high frequency and high speed copper clad laminate applications, thereby supporting the advancement of 5G and next generation electronic technologies.[1–4] However, conventional methods for enhancing the electrical conductivity of metals, such as purification and single-crystal growth, have reached their physical limits.[5] Recently, graphene/copper (Gr/Cu) composites have emerged as a promising solution.[3,4,6–9] Cao *et al.*[7] fabricated multilayered Gr/Cu composites, achieving ultrahigh electrical conductivity (117% IACS). It is well-established that a material's conductivity is governed by both carrier mobility and carrier concentration.[10] The enhanced electrical conductivity of Gr/Cu composites originates from two key aspects:

Increased carrier concentration: Cu has a higher carrier concentration than Gr.[11] When Gr contacts Cu, the difference in their work functions that Gr is higher than Cu drives electron transfer from Cu to Gr to align the Fermi levels,[11,12] resulting in n-type doping of Gr and significantly increasing the effective carrier concentration within the Gr layer. This is supported by Kelvin probe force microscopy measurements showing a lower contact potential difference for Gr compared to Cu in Gr/Cu systems.[3]

Preserved high carrier mobility: Gr exhibits ultra-high carrier mobility due to its linear Dirac-cone band dispersion near the Fermi level, where charge carriers behave as massless Dirac fermions with negligible effective mass.[13,14] Owing to the physisorption of Gr on the Cu substrate, where the Gr layer binds weakly to the Cu surface *via* van der Waals (vdW) interactions, the intrinsic band structure of Gr is preserved with only a rigid Fermi-level shift.[15] This minimal disruption allows the Gr's intrinsic ultrahigh carrier mobility to be maximally preserved.

Thus, by optimally combining high carrier concentration from carrier transfer and high mobility from the electronic structure, Gr/Cu composites achieve superior conductivity. However, interfacial charge transfer is limited by the intrinsic work functions difference between the pristine Gr and Cu, which constraining the potential for further increase in carrier concentration. Therefore, it is necessary to regulate the electronic structure of Gr to induce a more substantial Fermi level shift, while simultaneously preserving its characteristic high-mobility band structure.

[a]*State Key Lab of Metal Matrix Composites, School of Materials Science and Engineering, Shanghai Jiao Tong University, Shanghai 200240, China. E-mail: baixuebian@sjtu.edu.cn; mingyugong@sjtu.edu.cn; yliu23@sjtu.edu.cn*

[b]*Institute of Medical Robotics, Shanghai Jiao Tong University, Shanghai 200240, China*

© 2026 The Author(s). Published by the Royal Society of Chemistry

Open Access Article. Published on 28 January 2026. Downloaded on 3/7/2026 11:12:56 PM.
This article is licensed under a Creative Commons Attribution-NonCommercial 3.0 Unported Licence.

Chemical doping, is one of the most promising ways to tailor the electronic structure by carrier injection or extraction.[16,17] Chemical doping of Gr can be achieved through two primary approaches: surface charge-transfer doping (*via* physical/chemical adsorption) and substitutional doping. Surface doping preserves Gr's structural integrity but often leads to non-uniformity and poor environmental stability. Moreover, the weak interaction between surface dopants and Gr renders the doping effect vulnerable to external factors. In contrast, substitutional doping, which incorporates heteroatom directly into the Gr lattice, provides stable, controllable, and uniform modulation of properties.[16,18,19] It is therefore the preferred method for systematic studies.

Introducing heteroatom as dopants into Gr lattice would effectively modify the electronic structure of Gr and alter the carrier concentration. Such heteroatom dopants can be either electron donors or acceptors. Various nonmetallic elements including halogen (F, Cl, Br and I), N, B, S, P, and Si, have been incorporated into Gr lattice for efficient doping.[16] However, assessing the impact of substitutional doping on the Gr/Cu interface is complex due to the variety of doping elements and their multiple bonding configurations within the Gr lattice. For example, N typically forms three types of bonding structures: graphitic, pyridinic, and pyrrolic.[20,21] B can form two planar bonding configurations that are equivalent to graphitic and pyridinic.[22] Crucially, the different configurations induce different changes in carrier concentration. For instance, graphitic N can contribute 0.5 electrons to the π network of Gr, leading to an n-doping effect.[23] Conversely, pyridinic and pyrrolic N induce p-doping in Gr.[20] Moreover, defect-associated configurations like pyridinic and pyrrolic N inherently introduce vacancies and structural distortions into the lattice.

To fully elucidate the influence of substitutional doping, it is essential to decouple the doping effect into two components: the intrinsic electronic properties of the dopant atom, and the effect of vacancies or other point defects associated with non-graphitic configurations. Previous studies have demonstrated that the dangling bonds of vacancies would distort or destroy the Dirac point, resulting in a slight decline of the Fermi level and electron deficiency.[24,25] In this case, p-type doping is induced, and the carrier scattering would be enhanced.[24] Therefore, to design doped Gr/Cu composites with superior electrical transport performance, it is necessary to further investigate the regulation of dopant atom itself on the electronic properties of Gr/Cu.

In this work, we conducted a systematic first-principle study of different doped (O-, N-, B-, S-, P-, Br-, Si-) Gr on Cu (111). The chosen dopants represent commonly reported heteroatoms that have been experimentally demonstrated[16,26–32] to modify the electronic and interfacial properties of Gr. Among them, N and B are adjacent to carbon in the periodic table and readily substitute C atoms in graphene. Wei *et al.*[26] has synthesized N-doped Gr on Cu and Pt foils *via* chemical vapor deposition (CVD) using NH_3/CH_4 precursors, achieving doping concentrations up to 8–9 at%. B-doped graphene has been reported on Cu, Ni, and Co substrates using precursors such as boron powder or carborane molecules, leading to controllable p-type doping effects.[27,28] Other non-metallic dopants have also been experimentally realized.[29–32] This study focuses on the graphitic configuration, which allows for a more direct assessment of dopant atom itself and minimizes the confounding negative impacts of other defects. The binding energy and the formation energy were calculated to describe the stability and feasibility of doped Gr/Cu. Then, the charge density difference (CDD) and electron localization (ELF) were used to analyze the effect of different dopant atoms on interfacial bonding. Subsequently, we could screen candidate dopants based on their electronic properties, including band structure and electronic density of states. This screening prioritized elements that effectively modulate the Fermi level while maximally preserving band structure of Gr. The quantitative calculations of carrier concentration and mobility further enabled us to decouple the independent contributions of the dopant elements to these two parameters. Our work provides a systematic, first-principles comparison of the intrinsic interfacial electronic interactions induced by different substitutional dopants at the Gr/Cu interface. While previous studies often focus on single dopants, our unified approach decouples the effects on carrier concentration and mobility across multiple dopant species, offering microscopic insights to guide the optimization of conductivity and interfacial performance. Ultimately, these comprehensive results provide a theoretical guidance for the rational selection of optimal dopants, enabling the synergistic optimization of carrier concentration and carrier mobility, and thereby facilitating the design of high-performance Gr/Cu composite.

2 Computational details in DFT

All DFT calculations were conducted with the Vienna *ab initio* simulation package (VASP).[33] The Gr/Cu interface was modeled by a 4 × 4 × 1 supercell of Gr on Cu (111),[34] with a lattice mismatch below 3% after initial optimization. The model, shown in Fig. 1(a) and (b), used top-fcc stacking configuration, which is the most energy-favored arrangement. A dopant atom (O, N, B, S, P, Br, or Si) was introduced by substituting a single C atom in Gr, corresponding to about 3 at% doping concentration. The 4 × 4 lateral cell ensures a ≥10 Å separation between periodic dopant images, thereby minimizing dopant–dopant interactions and preserving the isolated-impurity limit. This

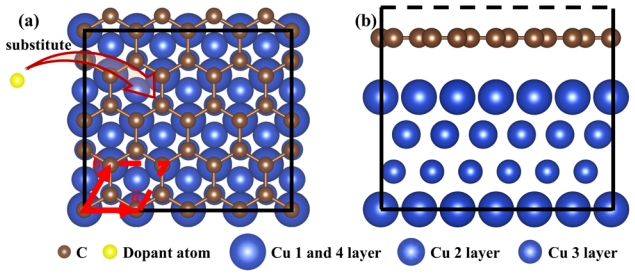

Fig. 1 (a) Top view for atomic models of pristine Gr on Cu (111), with the dopant atom (the yellow ball) substitutes carbon atom. For visualization clarity, a rectangular section of the hexagonal lattice is displayed by periodic boundary adjustment, while dashed lines represented periodic boundaries. (b) The side view for Gr/Cu.

 © 2026 The Author(s). Published by the Royal Society of Chemistry

Open Access Article. Published on 28 January 2026. Downloaded on 3/7/2026 11:12:56 PM. This article is licensed under a Creative Commons Attribution-NonCommercial 3.0 Unported Licence.

concentration was chosen based on our previous measurements of N-doped Gr/Cu, where peak conductivity was observed around ~3 at%.[11] A vacuum layer of ~20 Å was added along the *z*-axis to mitigate periodic interactions. The dipole correction[35] was neglected due to its negligible impact.

The projector augmented wave (PAW)[36] method was used to describe the electron–ion interactions, and the generalized gradient approximation (GGA) of Perdew–Burke–Ernzerhof (PBE)[37] was adopted for the exchange-correlation functional. The DFT-D3 empirical correction[38] was introduced to account for vdW interactions. A plane-wave energy cutoff of 450 eV was used. The convergence accuracy of the system total energy and the force per atom were 1.0×10^{-5} eV per atom and 0.02 eV Å^{-1}, respectively. The Brillouin zone was sampled by a $8 \times 8 \times 1$ Γ-centered k-mesh for optimization relaxation and $24 \times 24 \times 1$ for the electronic structure calculations. VASPKIT[39] was used for pre/post-processing, and VESTA[40] was used to visualization.

3 Results and discussion

3.1 Interface structure analysis

In order to obtain the energy-favored configuration, structural relaxation of the Gr/Cu interface is necessary. Table 1 shows the structural parameters of Gr/Cu and doped Gr/Cu after relaxation. The equilibrium interfacial distance between Gr and Cu layers ($d_{\text{Gr-Cu}}$) is 3.306 Å, agreeing with reported literature.[15] At low doping concentration, the equilibrium interfacial distances of all doped Gr/Cu exceed 3 Å, indicating that interfacial binding remains physisorbed interaction. However, doping induces in-plane lattice distortion due to the covalent radius mismatch between dopant and C atoms.[41] The magnitude of the lattice parameter after doping changes by about 0.04° in the γ directions. Meanwhile, the lattice constant *a* and *b* are changed by −0.02 Å to 0.04 Å depending on the difference radius of the dopant atoms and C atom. In fact, due to the low doping concentration, the doping of foreign atoms will induce more local structure changes rather than all regions. Therefore, we calculated the in-plane distortion of doped Gr/Cu and compared the bond lengths as well as the distance between the dopant atoms and the Cu layer. The results for the in-plane distortion and the corresponding structural parameters are presented in Fig. 2 and Table 1, respectively. The C–C bonds in Gr/Cu is 1.43 Å, which is consistent with the actual.[42,43] In this work, the distortion factor (ε_{xy}) is employed to quantitatively characterize the in-plane lattice distortion of the doped Gr/Cu system, as defined by eqn (1):

$$\varepsilon_{xy} = \frac{\sqrt{S_{\text{d-Gr/Cu}}} - \sqrt{S_{\text{Gr/Cu}}}}{\sqrt{S_{\text{Gr/Cu}}}} \quad (1)$$

where $S_{\text{d-Gr/Cu}}$ is local area around each atom in doped Gr, the area enclosed by the perpendicular bisector with the nearest neighboring atoms. Similarly, $S_{\text{Gr/Cu}}$ is the local area around the atoms in undoped Gr corresponding to $S_{\text{d-Gr/Cu}}$. The quantified in-plane distortion ε_{xy} in doped Gr/Cu was shown in Fig. 2(a)–(g), correlates with the covalent radius of dopant. Dopants larger than C, including B, S, P, Br, Si, induce lattice expansion from 4.64% to 11.71%, and their ε_{xy} values scale linearly with radius. Conversely, the smaller N atom causes lattice contraction ($\varepsilon_{xy} = -1.06\%$). An exception is O doping, which, despite its small radius, results in expansion due to its long O–C bond. This bond elongation also causes the O atom to shift upward compared to Gr plane where the $d_{\text{dopant-Cu}}$ is 3.457 Å. For other large dopants, the longer bonds cause them to move toward the Cu substrate, decreasing $d_{\text{dopant-Cu}}$ with increasing radius. Notably, the $d_{\text{dopant-Cu}}$ of S, P, Br, and Si falls below 2.5 Å (2.311, 2.255, 2.124 and 2.149, respectively), suggesting chemical bond formation. Combined Table 1 with Fig. 2(a)–(g), the dopants with larger atomic radius tend to reduce the $d_{\text{dopant-Cu}}$ and modify C-dopant bond lengths, indicating stronger interfacial interaction and a tendency toward chemisorption. In contrast, smaller dopants maintain larger separations, consistent with physisorbed interfaces.

Based on relaxation configuration, we calculated the formation energy (E_{f}) and the binding energy (E_{binding}). All the results are summarized in Table 2. The formation energy (E_{f}) was calculated using the following equation:[44]

$$E_{\text{f}} = E_{\text{tot}} - \sum_i n_i \mu_i = E_{\text{d-Gr/Cu}} + n_{\text{C}}\mu_{\text{C}} - E_{\text{Gr/Cu}} - n_{\text{d}}\mu_{\text{d}} \quad (2)$$

where E_{tot} is the total energy of system, n_i represents the number of elements *i*, μ_i represents the chemical potential of element *i*. n_{C} and n_{d} are the number of C and dopant atom, respectively. μ_{C} and μ_{d} are chemical potential of C and dopant atoms. The chemical potential of C atom is calculated as the cohesive energy per atom of Gr. Meanwhile, the chemical potentials of dopant atoms, including O, N, B, S, P, Br, Si, are calculated by the energy per atom of O_2, N_2, B_{12}, S_8, P_4, Br_2, Si, respectively. The E_{f} reflects the energy changing from the

Table 1 Structural parameters of doped Gr/Cu interface

	Interfacial distance/$d_{\text{Gr-Cu}}$ (Å)	$d_{\text{dopant-Cu}}$ (Å)	$d_{\text{C1-dopant}}$ (Å)	$d_{\text{C2-dopant}}$ (Å)	$d_{\text{C3-dopant}}$ (Å)
Gr/Cu	3.306	3.306	1.430	1.430	1.430
OGr/Cu	3.311	3.457	1.498	1.498	1.498
NGr/Cu	3.332	3.352	1.415	1.415	1.415
BGr/Cu	3.068	2.729	1.500	1.500	1.500
SGr/Cu	3.299	2.311	1.733	1.733	1.733
PGr/Cu	3.280	2.255	1.742	1.742	1.742
BrGr/Cu	3.434	2.124	1.997	1.997	1.995
SiGr/Cu	3.268	2.149	1.791	1.791	1.792

Open Access Article. Published on 28 January 2026. Downloaded on 3/7/2026 11:12:56 PM.
This article is licensed under a Creative Commons Attribution-NonCommercial 3.0 Unported Licence.

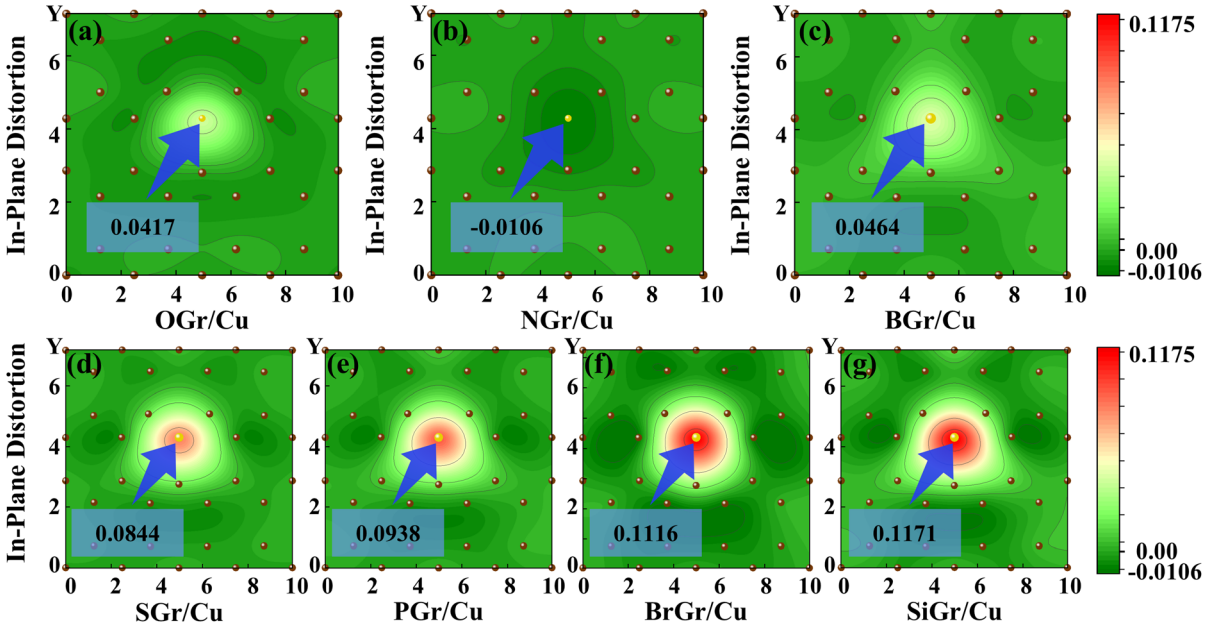

Fig. 2 The in-plane distortion ε_{xy} of doped Gr/Cu systems: (a) OGr/Cu, (b) NGr/Cu, (c) BGr/Cu, (d) SGr/Cu, (e) PGr/Cu, (f) BrGr/Cu, and (g) SiGr/Cu.

Table 2 The formation energy (E_f) and the binding energy ($E_{binding}$) of various doped Gr/Cu interface models

	Weakly-interacting				Strongly-interacting			
	Gr/Cu	OGr/Cu	NGr/Cu	BGr/Cu	SGr/Cu	PGr/Cu	BrGr/Cu	SiGr/Cu
E_f/(eV)	—	2.76	0.78	−1.07	2.98	−2.03	11.12	2.06
$E_{binding}$/(eV)	−2.68	−2.80	−2.81	−3.33	−3.19	−4.00	−3.33	−4.24

doping process. Significantly, the formation energy of BrGr/Cu (E_f is 11.12 eV) is much more than other doped Gr/Cu, indicating that it needs more energy and is more difficult in preparation. Therefore, the impracticality of the BrGr/Cu system disqualifies Br as a suitable dopant for this application.

The binding energy ($E_{binding}$) was calculated by eqn (3):[45]

$$E_{binding} = E_{d\text{-}Gr/Cu} - E_{d\text{-}Gr} - E_{Cu} \quad (3)$$

where$E_{d\text{-}Gr/Cu}$, $E_{d\text{-}Gr}$, E_{Cu} are the total energy of doped Gr/Cu interface, doped Gr, and Cu layer, respectively. The binding energy ($E_{binding}$) reflects the interfacial bond strength and the stability of the structure of doped Gr/Cu, where a negative value signifies stability. The calculated $E_{binding}$ for Gr/Cu is −2.68 eV, agreeing well with previously published results.[46,47] All doped structures are stable, and doping universally strengthens the interfacial bonding strength between the Gr and Cu layer. The weakly interacting dopant atoms, including O and N, lead to only a modest enhancement, while the strongly interacting dopant atoms have a more significant enhancement.

3.2 Electronic structure analysis

The observed lattice distortions and the variations in interfacial bonging are fundamentally influenced by the resultant changes in the electronic structure at the Gr/Cu interface. To uncover this electronic level origin, the charge density difference (CDD), the planar-averaged CDD and electron localization function (ELF) were calculated and showed in Fig. 3. The CDD of doped Gr/Cu is calculated by the following equation:[47]

$$\Delta\rho = \rho_{d-Gr/Cu} - \rho_{Gr/Cu} - \rho_{Cu} \quad (4)$$

where $\rho_{d-Gr/Cu}$, $\rho_{Gr/Cu}$, ρ_{Cu} are the charge densities of the doped-Gr/Cu, doped Gr and Cu layers, respectively. Fig. 3(a) presents the 2D CDD on the (010) plane crossing the dopant atom in doped Gr/Cu. The red and blue regions correspond to charge accumulation and depletion, respectively, where pronounced charge redistribution signifies strong interfacial interactions. Fig. 3(b) illustrates the planar-averaged CDD of pristine Gr/Cu and doped Gr/Cu interfaces, enabling a more intuitive and semi-quantitative analysis of charge transfer and interfacial coupling. For the pristine Gr/Cu interface (Fig. 3(a)), the CDD exhibits a symmetric and uniform distribution at the interface. In contrast, both OGr/Cu and NGr/Cu display stronger charge accumulation and depletion between Gr and the Cu layers, as evidenced by their higher peak values (0.38 and 0.45, respectively) compared to that of pristine Gr/Cu (0.27) in Fig. 3(b). These results, consistent with Fig. 3(a), indicate that O and N doping enhance the interfacial interaction. However, OGr/Cu and NGr/Cu still remain symmetrical and confined to the

 © 2026 The Author(s). Published by the Royal Society of Chemistry

Open Access Article. Published on 28 January 2026. Downloaded on 3/7/2026 11:12:56 PM.
This article is licensed under a Creative Commons Attribution-NonCommercial 3.0 Unported Licence.

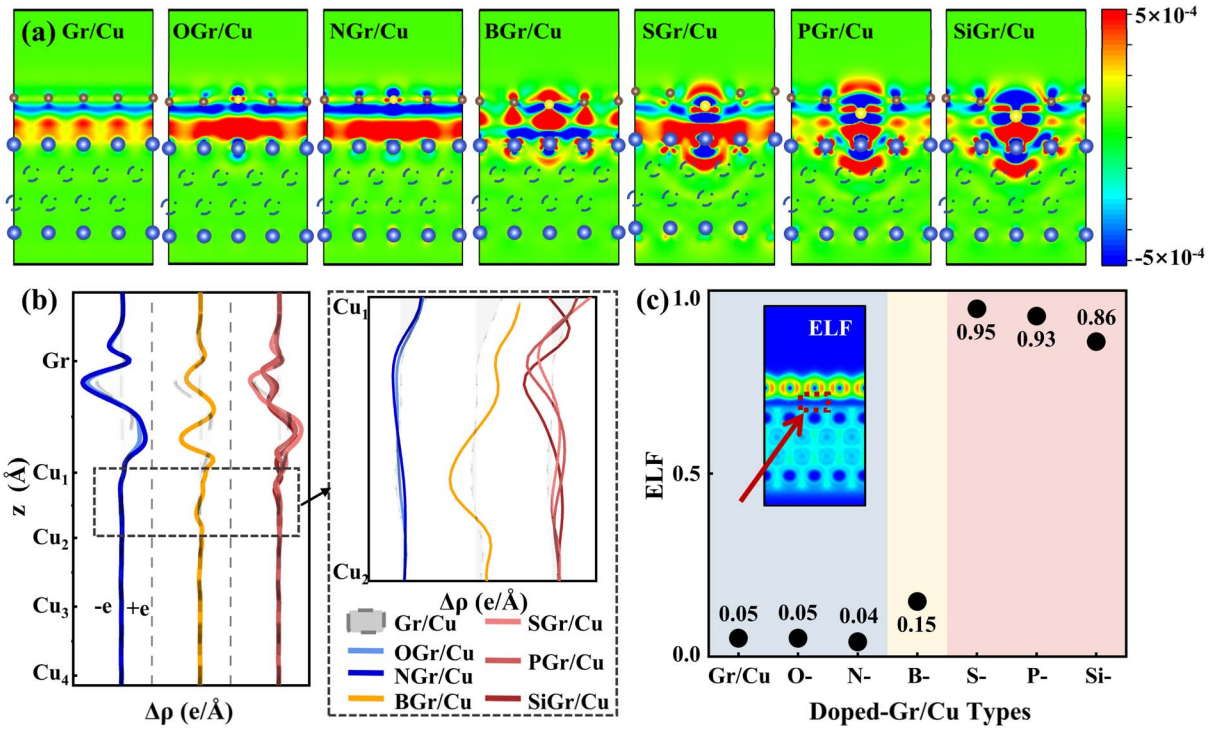

Fig. 3 (a) The two-dimensional slicing plane for CDD of doped Gr/Cu. Color bar scale: ±5 × 10−4 e Å^{-3}. (b) The planar-averaged charge density differences along vertical direction for the doped Gr/Cu. (c) Corresponding ELF values of doped Gr/Cu, with an inset showing a two-dimensional display at the interface (numbers denote the maximum ELF value between dopants and Cu layer).

interface, preserving the sp^2 hybridization and maintaining physisorbed interaction. For BGr/Cu, B doping introduces both enhanced charge accumulation at the interface and localized charge redistribution around the dopant atom. Similarly, SGr/Cu, PGr/Cu, and SiGr/Cu demonstrate an expanded region of electronic interaction around the dopant sites. This is particularly evident in Fig. 3(b), where strong charge redistribution is observed not only at the interface but also between the first and second Cu layers, further confirming the strong interfacial interaction. The ELF, which describes the degree of electron localization and covalent bonding strength (with values normalized between 0 and 1), offers complementary insights. Fig. 3(c) shows the ELF values at the interface of doped Gr/Cu, the inset figure is a schematic of the ELF, whose value is chosen between the dopant atom and the Cu atom below it. The ELF results agree well with the CDD analysis that the low ELF values for OGr/Cu (0.05) and NGr/Cu (0.04) are similar to pristine Gr/Cu (0.05), indicating electron delocalization. Conversely, SGr/Cu (0.95), PGr/Cu (0.93), and SiGr/Cu (0.86) exhibit high ELF values, signifying strong covalent bonding. The moderate value for BGr/Cu (0.15) suggests an intermediate, weakly chemical bond.

To comprehensively explore the detailed mechanisms by which doping influences the electrical properties, the band structures and the projected density of states (PDOS) for doped Gr/Cu were calculated as presented in Fig. 4 and 5, respectively. Fig. 4(a) is a schematic of band structure evolution in Gr with Cu substrate and dopant introduction. The band structure of suspended Gr (Fig. 4(b), blue dashed line) exhibits a characteristic Dirac cone with linear dispersion and zero bandgap near the Fermi level,[48] which ensures its ultra-high carrier mobility that can reach up to 10^6 cm^2 s^{-1} V^{-1}.[49,50] When supported on Cu, the Fermi level shifts upward ($\Delta E = -0.25$ eV), indicating n-type doping due to electron transfer from the substrate to Gr as depicted in Fig. 4(b). According to the equation $E_F = \hbar v_F \sqrt{\pi n}$,[7,11,46] the shift of the Fermi level alters the carrier concentration. The introduction of doping significantly influences the electronic state, specially, leading to a shift of the Dirac point, and further modifying the carrier concentration. Moreover, doping causes an obvious bandgap, leads to local distortion, and disrupts the symmetry of Gr,[51] resulting in a destroyed Dirac cone due to the enhanced interfacial interaction.[15] The full band structures of doped Gr/Cu are shown in Fig. 4(c)–(h). NGr/Cu (Fig. 4(d)) and BGr/Cu (Fig. 4(e)) maintain a relatively intact Dirac cone, but open the bandgap. NGr/Cu shows a strong n-type shift ($\Delta E = -0.7$ eV) compared to Gr/Cu, while BGr/Cu exhibits a p-type shift ($\Delta E = 0.24$ eV) due to the reverse doping effect from B dopant and the Cu layer. In contrast, O, S, P and Si doping severely distort or destroy the Dirac cone as shown in Fig. 4(c) and (f)–(h). Fig. 5 presents the projected density of states (PDOS) for the doped Gr/Cu systems. In addition to the C-2p orbital, the dopant-2p orbital also contribute to the energy bands near the Fermi level. Obviously, The NGr/Cu interface exhibits n-type semiconducting characteristics and BGr/Cu interface exhibits p-type semiconducting characteristics in the doped interface systems, as shown in Fig. 5(b) and (c), respectively. For the BGr/Cu, the C-2p, B-2p and Cu-3d orbitals overlap at −2 eV ∼ −3 eV, which means stronger

Open Access Article. Published on 28 January 2026. Downloaded on 3/7/2026 11:12:56 PM.
This article is licensed under a Creative Commons Attribution-NonCommercial 3.0 Unported Licence.

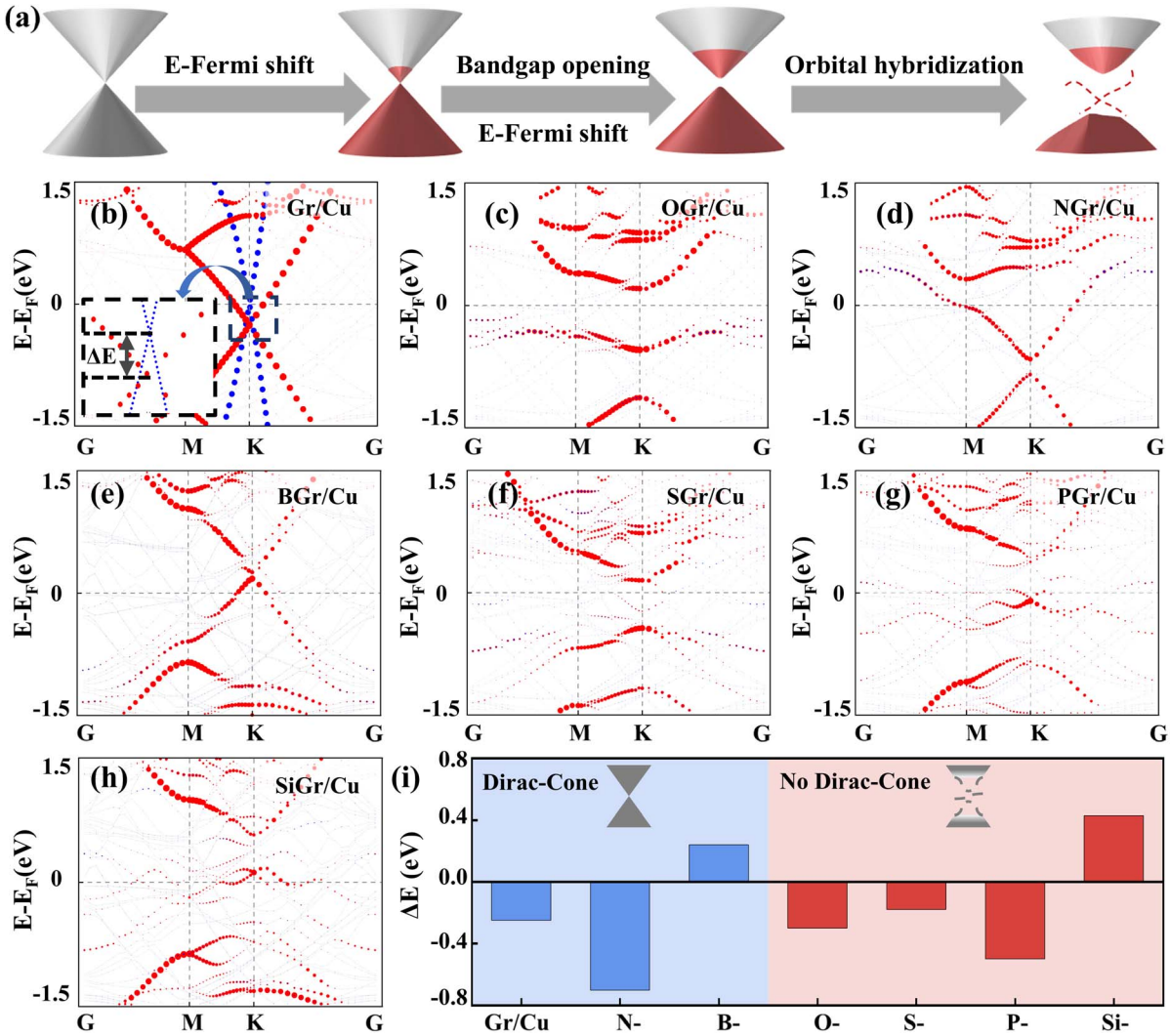

Fig. 4 (a) Schematic representation of Gr band structure evolution with dopant introduction. (b)–(h) Band structures of Gr/Cu (the blue dashed line represent the band structure of Gr), OGr/Cu, NGr/Cu, BGr/Cu, SGr/Cu, PGr/Cu, SiGr/Cu, respectively. (i) Fermi level shifts (ΔE) in pristine and doped Gr/Cu interfaces.

interfacial interaction compared to NGr/Cu. However, the interface interaction does not significantly change the properties of the doped Gr, both NGr/Cu and BGr/Cu exhibit Dirac cone. For OGr/Cu, the O-2s orbital peaks between 2 eV and 3 eV indicate that the impurity levels appearing in the Fig. 5(a) are mainly contributed by O dopant. Moreover, the peaks of Cu-3d orbitals and O-2p orbitals overlap at −2.5 eV and −4.5 eV, accompanied by orbital hybridization, resulting in the destruction of Dirac cone of OGr/Cu. For SGr/Cu, PGr/Cu and SiGr/Cu as shown in Fig. 5(d)–(f), the Cu-3d and dopant-2p exhibit orbital hybridization in valence band. The destruction of the Dirac cone means the carrier mobility is severely reduced for these systems. Moreover, the total density of states (TDOS) and PDOS for the pristine Gr/Cu system was also calculated in this work, as shown in Fig. S1. No obvious orbital hybridization is observed between Cu and C atoms, indicating the absence of covalent bonding, which is consistent with the analysis of the Gr/Cu models above. It can be seen that in the Gr/Cu interface, the energy bands near the Fermi level are mainly contributed by the C-2p orbital, while the Cu-3d orbital is primarily concentrated in the valence band. The interaction between Gr and the Cu substrate shifts the Fermi level into the conduction band, resulting in n-type semiconductor characteristics, and the Dirac cone of Gr remains intact. The intact Dirac cone preserve the high carrier mobility of Gr, while the destruction of the Dirac cone means the carrier mobility is severely reduced. Consequently, NGr/Cu and BGr/Cu, which preserve the Dirac cone morphology, are expected to maintain higher mobility, with NGr/Cu offering the highest carrier concentration due to the most negative ΔE (Fig. 4(i)).

3.3 Carrier mobility and carrier concentration

To critically evaluate the relative advantages of N doping *versus* B doping on carrier concentration and mobility, we performed quantitative calculations of these parameters specifically for NGr/Cu and BGr/Cu systems. The carrier transport performance of the doped Gr/Cu at room temperature is estimated by the

 © 2026 The Author(s). Published by the Royal Society of Chemistry

Open Access Article. Published on 28 January 2026. Downloaded on 3/7/2026 11:12:56 PM.
This article is licensed under a Creative Commons Attribution-NonCommercial 3.0 Unported Licence.

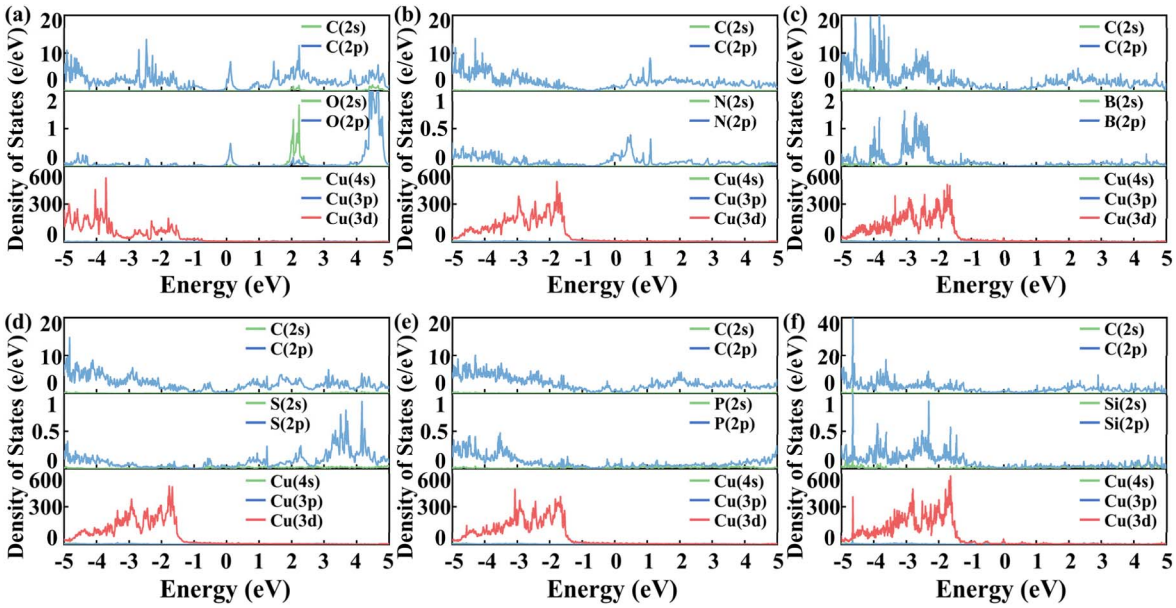

Fig. 5 The projected density of states for different doped Gr/Cu composites: (a) OGr/Cu, (b) NGr/Cu, (c) BGr/Cu, (d) SGr/Cu, (e) PGr/Cu, (f) SiGr/Cu. All graphs include each atom and correspond to their respective orbitals.

acoustic phonon limited method, based on the deformation potential theory proposed by Bardeen and Shockley. We first transform the original hexagonal unit cell of Gr/Cu into the rectangular unit cell. Generally, the carrier mobility, μ_{2D}, of the 2D materials, with a view to studying the properties of migration of electrons and holes, can be obtained as follows:[52–54]

$$\mu_{2D} = \frac{e\hbar^3 C_{2D}}{k_B T m^* m^d E_1{}^2} \tag{5}$$

where m^* is carrier effective mass along transport direction using $m^* = \hbar^2(\partial^2 E/\partial k^2)^{-1}$ and $m_d = \sqrt{m_x^* m_y^*}$ is the average effective mass. $E_1 = \Delta E_{edge}/(\Delta l/l_0)$ is the deformation potential (DP) constant, defined as the shift of band edges induced by strain. Here, ΔE_{edge} represents the energy difference about conduction band minimum (CBM) or valence band maximum (VBM) with the lattice applied y proper dilatation or compression. l_0 and Δl are the lattice constant along the x or y direction and their deformation, corresponding. In the 2D materials, in-plane stiffness, C_{2D}, can be calculated using $C_{2D} = [\partial^2 E/\partial(\Delta l/l_0)^2]/S_0$, where E and S_0 stand for the total energy and the area of the xy plane for the supercell, respectively. Besides, e, $\hbar$, k_B, and T are electronic quantity, reduced Planck constant, Bolzban constant, and 300 K, respectively.

The calculated carrier mobilities of NGr/Cu and BGr/Cu are summarized in Table 3 and Fig. 6(a). The results revealed that the carrier mobilities of NGr/Cu and BGr/Cu show anisotropy between electron and hole. Consistent with their n-type and p-type doping characters, the mobility corresponds to electron transport for NGr/Cu and hole transport for BGr/Cu. NGr/Cu has the electron mobilities of 2.74×10^5 and 2.33×10^5 cm^2 s^{-1} V^{-1} in the zigzag and armchair directions, respectively, which are both more than the hole mobility of BGr/Cu. According to the formula of μ_{2D}, the greatly enhanced electron mobility in the NGr/Cu mainly results from the lowest the deformation potential (DP) compared to the BGr/Cu. Fig. 2(b) and (c) shows the in-plane distortion of NGr/Cu and BGr/Cu are 7.1% and 14.1% (the sum of all atomic distortions in the plane), respectively. The greater in-plane lattice distortion in BGr/Cu and the localized states induced by B doping (Fig. 3(a)) contribute to enhanced carrier scattering and consequently degraded mobility in BGr/Cu.

According to the equation $E_F = \hbar v_F \sqrt{\pi n}$, the carrier concentration is positively correlated with the shift of Fermi level. This relationship, however, assumes Gr's linear dispersion relation. When doping induced bandgap opening, the linearity may be disrupted. To address this nonlinear regime,

Table 3 Calculated carrier mobility ($\mu_i \times 10^4$ cm^2 s^{-1} V^{-1}) in doped Gr/Cu along x (Zigzag-Chain) and y (Armchair-Chain) directions at 300 K

	C_{2D-x} (J m^{-2})	C_{2D-y}	$E_{1-x}(J)$	E_{1-y}	m_e	μ_x	μ_y
Electrons							
NGr/Cu	275.58	283.86	-3.67×10^{-19}	-4.04×10^{-19}	0.093	27.36	23.25
BGr/Cu	265.37	268.98	-4.73×10^{-19}	-5.29×10^{-19}	0.064	7.49	6.08
Holes							
NGr/Cu	275.58	283.86	-3.90×10^{-19}	-3.754×10^{-19}	0.069	12.63	14.06
BGr/Cu	265.37	268.98	-6.44×10^{-19}	-6.008×10^{-19}	0.089	7.32	8.52

Open Access Article. Published on 28 January 2026. Downloaded on 3/7/2026 11:12:56 PM.
This article is licensed under a Creative Commons Attribution-NonCommercial 3.0 Unported Licence.

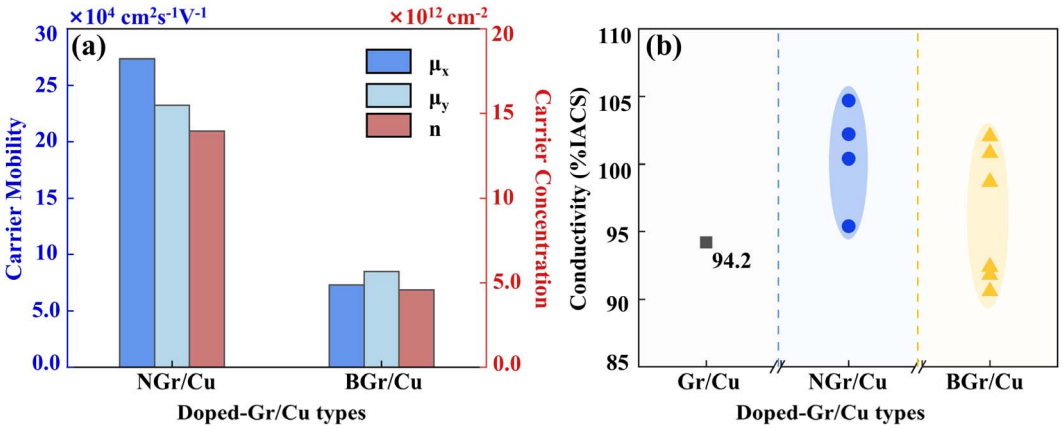

Fig. 6 Carrier mobility (μ) and carrier concentration (n) of NGr/Cu, BGr/Cu, and BNGr/Cu along different directions. (b) Electrical conductivity of Gr/Cu, NGr/Cu,[11] and BGr/Cu[57] in experiment.

eqn (6) was derived under parabolic band conditions to calculate carrier concentration. The m^* is carrier effective mass. ΔE is a shift of the Fermi level and $\hbar$ is reduced Planck constant. The computational results were detailed in Table 4 and Fig. 6(a), with the full derivation process provided in SI. The results are consistent with the experiment.[55,56] NGr/Cu has higher carrier concentration due to the combined doping effects from N dopant and Cu. Although electrons transfer from Cu to Gr occurs in BGr/Cu, B doping induces holes, resulting in a lower carrier concentration in BGr/Cu. This trend is reflected in the experimental conductivities shown in Fig. 6(b).[11,57] The peak conductivity of NGr/Cu reaches 104.7% IACS, an 11.14% enhancement over pristine Gr/Cu (94.2% IACS). BGr/Cu also shows a peak conductivity (102.3% IACS) exceeding that of Gr/Cu, its overall performance is inferior to N-doping. Both theoretical and experimental analyses confirm that N doping is the optimal strategy for synergistically regulating carrier concentration and mobility. It should be emphasized, however, that the present calculations are performed under an idealized single-atom substitutional doping. In practical fabrication processes, additional structural infects, such as grain boundaries or non-graphitic N configurations (*e.g.*, pyridinic N), are often present and can introduce extra carrier scattering, thereby reducing the measured conductivity relative to the ideal case. These effects are not explicitly considered in our current framework. Consequently, the conductivity values predicted here should be regarded as the intrinsic upper limit achievable for defect-free Gr/Cu interfaces under substitutional doping, serving as a benchmark for guiding experimental optimization and defect control strategies.

$$n = \frac{m^*}{2\pi\hbar^2}\Delta E \tag{6}$$

Table 4 Calculated carrier concentration ($n \times 10^{12}$ cm^{-2}) in doped Gr/Cu

	m^*	ΔE (eV)	n
NGr/Cu	0.095	−0.70	13.96/7 (ref. 55)
BGr/Cu	0.089	0.24	4.59/2.27 (ref. 56)

4 Conclusions

Ultra-high-conductivity Cu materials are critically needed in advanced electrical and electronic fields, including high-frequency communication, 5 G infrastructure, integrated circuits, and power transmission. Enhancing Cu conductivity can significantly reduce energy loss, minimize device size and weight, and overcome performance degradation due to electron scattering at scaled-down interconnects. Doped Gr/Cu composites represent a promising strategy to improve interfacial electron coupling and overall conductivity of Cu-based systems. In this work, the effects of various doping elements (O, N, B, S, P, Br and Si) on the interfacial and electrical properties of Gr/Cu composites were investigated systematically by using the first-principles calculations. Our findings reveal competing effects of doping:

(i) Interfacial binding enhancement: doping can enhance the interfacial binding strength, where the interaction generally intensifies as the atomic radius increases. However, an overly strong interaction between the dopant and Cu atoms introduces localized electronic states, thereby enhancing carrier scattering and resulting in reduced mobility.

(ii) Carrier concentration modulation: doping effectively modulates the electronic structure of Gr by injecting either electrons or holes, thereby tuning the carrier concentration.

N doping was found to achieve an optimal balance between carrier concentration (1.4×10^{13} cm^{-2}) and carrier mobility (2×10^5 cm^2 s^{-1} V^{-1}). Consequently, nitrogen (N) stands out as the most suitable dopant for achieving a breakthrough in high-conductivity Gr/Cu composites. Future work could include experimental validation of the predicted optimal dopant configurations, along with systematic studies on the influence of doping concentration, common interfacial defects, and interfacial modification on carrier transport. Such efforts would not only substantiate the present theoretical framework but also guide the practical design of high-conductivity Gr/Cu composites.

Author contributions

Xinsi Zhao: data curation (lead); formal analysis (lead); methodology (lead); writing – original draft (lead). Boan Zhong:

 © 2026 The Author(s). Published by the Royal Society of Chemistry

Open Access Article. Published on 28 January 2026. Downloaded on 3/7/2026 11:12:56 PM.
This article is licensed under a Creative Commons Attribution-NonCommercial 3.0 Unported Licence.

methodology (equal); validation (equal); visualization (equal). Baixue Bian: methodology (equal); validation (equal); writing – review & editing (equal). Jiamiao Ni: methodology (equal); validation (equal); Mingyu Gong: conceptualization (equal); funding acquisition (lead); methodology (equal); formal analysis (equal); investigation (equal); validation (equal); writing – review & editing (lead). Yue Liu: conceptualization (equal); methodology (equal); validation (equal). Tongxiang Fan: project administration (lead); software (supporting); supervision (supporting).

Conflicts of interest

There are no conflicts to declare.

Data availability

The data supporting the findings of this study are available from the corresponding authors upon reasonable request.

Supplementary information (SI): DOS of the Gr/Cu interface (Fig. S1); and derivation of equation used in carrier concentration in doped Gr/Cu. See DOI: https://doi.org/10.1039/d5ra09101b.

Acknowledgements

This work was supported by the National Natural Science Foundation of China (No. 52201161).

Notes and references

1 Y. Zhou, *Acc. Mater. Res.*, 2021, **2**, 306–310.
2 R. A. Maniyara, D. Rodrigo, R. Yu, J. Canet-Ferrer, D. S. Ghosh, R. Yongsunthon, D. E. Baker, A. Rezikyan, F. J. García de Abajo and V. Pruneri, *Nat. Photonics*, 2019, **13**, 328–333.
3 S. He and D. Xiong, *J.Nonferrous Met.*, 2023, **33**(5), 1349–1377.
4 B. Gwalani, X. Li, A. Nittala, W. Choi, M. Reza-E-Rabby, J. E. Atehortua, A. Bhattacharjee, M. Pole, J. Silverstein, M. Song and K. Kappagantula, *Mat. Design*, 2024, **237**, 112555.
5 M. Ajmal, S. Lee, Y. C. Cho, S. J. Kim, S. E. Park, C. R. Cho and S. Y. Jeong, *CrystEngComm*, 2012, **14**, 1463–1467.
6 X. Zhang, N. Zhao and C. He, *Prog. Mater. Sci.*, 2010, **113**, 100672.
7 M. Cao, D. B. Xiong, L. Yang, S. Li, Y. Xie, Q. Guo, Z. Li, H. Adams, J. Gu, T. Fan, X. Zhang and D. Zhang, *Adv. Funct. Mater.*, 2019, **29**, 1806792.
8 J. Yu, L. Wang, Y. Guan, B. Shao, Y. Zong and C. Pt, *Composites, Part A*, 2024, **185**, 108345.
9 C. Pan, A. P. S. Gaur, M. Lynn, M. P. Olson, G. Ouyang and J. Cui, *AIP Adv.*, 2022, **12**, 015310.
10 M. Hofmann, Y. P. Hsieh, K. W. Chang, H. G. Tsai and T. T. Chen, *Sci. Rep.*, 2015, **5**, 17393.
11 Y. Wang, B. Zhong, J. Ni, J. Song, Y. Huang, S. Yao, Y. Liu and T. Fan, *Scr. Mater.*, 2024, **239**, 115797.
12 G. Giovannetti, P. A. Khomyakov, G. Brocks, V. M. Karpan, J. van den Brink and P. J. Kelly, *Phys. Rev. Lett.*, 2008, **101**, 026803.
13 A. H. Castro Neto, F. Guinea, N. M. R. Peres, K. S. Novoselov and A. K. Geim, *Rev. Mod. Phys.*, 2009, **81**, 109.
14 N. O. Weiss, H. Zhou, L. Liao, Y. Liu, S. Jiang, Y. Huang and X. Duan, *Adv. Mater.*, 2012, **24**, 5782–5825.
15 M. Yang, Y. Liu, T. Fan and D. Zhang, *Prog. Mater. Sci.*, 2020, **110**, 100652.
16 Z. Hu, Y. Zhao, W. Zou, Q. Lu, J. Liao, F. Li, M. Shang, L. Lin and Z. Liu, *Adv. Funct. Mater.*, 2022, **32**, 2203179.
17 S. Ullah, Q. Shi, J. Zhou, X. Yang, H. Q. Ta, M. Hasan, N. M. Ahmad, L. Fu, A. Bachmatiuk and M. H. Rümmeli, *Adv. Mater. interfaces.*, 2020, **7**, 2000999.
18 L. Ma, W. Ren and H. Cheng, *Acta Phys.-Chim. Sin.*, 2022, **38**(1), 2012080.
19 Y. Zhou, X. He and M. Li, *AIP Adv.*, 2025, **15**, 010701.
20 S. Jalili and R. Vaziri, *Mol. Phys.*, 2011, **109**, 687–694.
21 Q. Jia, B. Zhong, S. Wang, Z. Yue, Y. Liu and X. Wang, *Phys. Status Solidi RRL*, 2025, **19**, 2400165.
22 S. Agnoli and M. Favaro, *J. Mater. Chem. A*, 2016, **4**, 5002–5025.
23 J. Zhang, C. Zhao, N. Liu, H. Zhang, J. Liu, Y. Q. Fu, B. Guo, Z. Wang, S. Lei and P. Hu, *Sci. Rep.*, 2016, **6**, 28330.
24 Y. Liu, L. An and L. Gong, *Mod. Phys. Lett. B*, 2018, **32**, 1850139.
25 E. Zaminpayma, M. E. Razavi and P. Nayebi, *Appl. Surf. Sci.*, 2017, **414**, 101–106.
26 D. Wei, Y. Liu, Y. Wang, H. Zhang, L. Huang and G. Yu, *Nano lett.*, 2009, **9**(5), 1752–1758.
27 X. Li, L. Fan, Z. Li, K. Wang, M. Zhong, J. Wei, D. Wu and H. Zhu, *Adv. Energy Mater.*, 2012, **2**, 425.
28 D. Y. Usachov, A. V. Fedorov, A. E. Petukhov, O. Y. Vilkov, A. G. Rybkin, M. M. Otrokov, A. Arnau, E. V. Chulkov, L. V. Yashina, M. Farjam, V. K. Adamchuk, B. V. Senkovskiy, X. C. Laubschat and D. V. Vyalikh, *ACS Nano*, 2015, **9**(7), 7314–7322.
29 M. Ovezmyradov, I. V. Magedov, L. V. Frolova, G. Chandler, J. Garcia, D. Bethke, E. A. Shaner and N. G. Kalugin, *J. Nanosci. Nanotechnol.*, 2015, **15**, 4883.
30 A. Ganguly, S. Sharma, P. Papakonstantinou and J. Hamilton, *J. Phys. Chem. C*, 2011, **115**(34), 17009–17019.
31 L. Guo and T. Li, *Sens. Actuators, B*, 2018, **255**, 2258–2263.
32 M. Hasan, W. Meiou, Y. Liu, S. Ullah, H. Q. Ta, L. Zhao, R. G. Mendes, Z. P. Malik, N. Ahmad, Z. Liu and M. H. Rummeli, *RSC Adv.*, 2019, **9**, 13527.
33 G. Kresse and J. Furthmüller, *Phys. Rev. B: Condens. Matter Mater. Phys.*, 1996, **54**, 11169.
34 L. Zhang, J. Dong and F. D, *J. Phys. Chem. Lett.*, 2014, **15**, 758–765.
35 L. Bengtsson, *Phys. Rev. B: Condens. Matter Mater. Phys.*, 1999, **59**, 12301.
36 G. Kresse and D. Joubert, *Phys. Rev. B: Condens. Matter Mater. Phys.*, 1999, **59**, 1758.
37 J. P. Perdew, K. Burke and M. Ernzerhof, *Phys. Rev. Lett.*, 1996, **77**, 3865.

Open Access Article. Published on 28 January 2026. Downloaded on 3/7/2026 11:12:56 PM.
This article is licensed under a Creative Commons Attribution-NonCommercial 3.0 Unported Licence.

38 S. Grimme, J. Antony, S. Ehrlich and H. Krieg, *J. Chem. Phys.*, 2010, **132**, 154104.
39 V. Wang, N. Xu, J. C. Liu, G. Tang and W. T. Geng, *Comput. Phys. Commun.*, 2021, **267**, 108033.
40 K. Momma and F. Izumi, *J. Appl. Crystallogr.*, 2011, **44**, 1272–1276.
41 Y. Liao, R. He, W. Pan, Y. Li, Y. Wang, J. Li and Y. Li, *Chem.–Eng. J.*, 2023, **464**, 142669.
42 P. Avouris, *Nano Lett.*, 2010, **10**, 4285–4294.
43 Y. Qu, J. Ding, H. Fu, H. Chen and J. Peng, *Appl. Surf. Sci.*, 2021, **542**, 148763.
44 C. G. Van de Walle and J. Neugebauer, *J. Appl. Phys.*, 2004, **95**, 3851–3879.
45 L. Ferrighi, M. I. Trioni and C. Di Valentin, *J. Phys. Chem. C*, 2015, **119**, 6056–6064.
46 B. Zhong, J. Ni, Q. Zhang, J. Song, Y. Liu, M. Gong and T. Fan, *J. Appl. Phys.*, 2024, **136**, 055107.
47 S. He, B. Liu, Z. Pei, X. Zhang, B. Liu and D. Xiong, *J. Appl. Phys.*, 2023, **134**, 075104.
48 H. Şahin, S. Cahangirov, M. Topsakal, E. Bekaroglu, E. Akturk, R. T. Senger and S. Ciraci, *Phys. Rev. B: Condens. Matter Mater. Phys.*, 2009, **80**, 155453.
49 N. Weiss, H. Zhou, L. Liao, Y. Liu, S. Jiang, Y. Huang and X. Duan, *Adv. Mater.*, 2012, **24**, 5782–5825.
50 Y. Xue, B. Wu, Q. Bao and Y. Liu, *Small*, 2014, **15**, 2975–2991.
51 N. Liu, S. Zhou and J. Zhao, *Acta Phys.-Chim. Sin.*, 2019, **35**, 1142–1149.
52 S. Bruzzone and G. Fiori, *Appl. Phys. Lett.*, 2011, **99**, 222108.
53 T. Liang, C. Hu, M. Lou, Z. Feng, D. Wang, X. Cai and L. Lin, *Langmuir*, 2023, **39**, 10769–10778.
54 Z. Yan, R. Gao, M. Chang, S. Qi and X. Xu, *Magn. Magn. Mater*, 2020, **496**, 165966.
55 L. Zhao, M. Levendorf, S. Goncher, T. Schiros, L. Pálová, A. Zabet-Khosousi, K. T. Rim, C. Gutiérrez, D. Nordlund, C. Jaye, M. Hybertsen, D. Reichman, G. Flynn, J. Park and A. Pasupathy, *Nano Lett.*, 2013, **13**, 4659–4665.
56 M. Scardamaglia, C. Struzzi, S. Osella, N. Reckinger, J.-F. Colomer, L. Petaccia, R. Snyders, D. Beljonne and C. Bittencourt, *2D Mater.*, 2016, **3**, 011001.
57 M. Yang, T. Li, W. Liu, Y. Wang, H. Hou, CN 112877562 B, 2022.

 © 2026 The Author(s). Published by the Royal Society of Chemistry